J. Fluid Mech. (2003), *vol.* 492, *pp.* 363–379. © 2003 Cambridge University Press
DOI: 10.1017/S002211200300572X Printed in the United Kingdom

Inertial instabilities of fluid flow in precessing spheroidal shells

By S. LORENZANI AND A. TILGNER

Institute of Geophysics, University of Göttingen, Herzberger Landstr. 180, D-37075 Göttingen, Germany

(Received 18 February 2002 and in revised form 26 February 2003)

As a model for the precession-driven motion in the Earth's core, the flow of incompressible fluid inside a spheroidal shell with imposed rotation and precession is investigated by direct numerical simulation. In one set of simulations, free-slip boundary conditions are used in order to isolate inertial instabilities. These occur as triad resonances involving pairs of inertial modes which have the form of columnar vortices. The simulations reproduce the phenomenon of 'resonant collapses' in which the excited modes periodically grow and suddenly decay into turbulence. The experiments of Malkus (1968) are simulated using a hyperviscosity. A hysteretic transition towards developed turbulence observed in one of these experiments can be interpreted as a feature of the basic laminar flow rather than the instability itself. A similar transition can be excluded for Earth's parameters.

1. Introduction

Precession has long been recognized as a possible driving mechanism for the geodynamo (Bullard 1949); but the basic laminar precession-driven flow in an ellipsoidal shell is nearly toroidal and thus inefficient in generating a magnetic field. Only unstable precession-driven flow is possibly a dynamo. We therefore wonder whether precession causes a laminar or unstable or even turbulent flow inside the Earth's core. A series of experiments (Malkus 1968; Vanyo *et al.* 1995; Vanyo & Dunn 2000) has demonstrated how laminar, weakly time-dependent, and highly turbulent flows can all be generated by precession. The numerical study of the associated instabilities has only started recently (Tilgner & Busse 2001; Lorenzani & Tilgner 2001). Hydrodynamic instabilities can be classified into two broad groups. They are either 'viscous' and exist only for a viscosity different from zero, or they are 'inertial' and occur also in an ideal fluid. The instabilities studied thus far all exist in spherical geometry. In a sphere, a simple solid-body rotation is a solution of the equation of motion for an ideal fluid. A solid-body rotation is a stable flow so that the instabilities simulated up to now are all due to modifications of the flow introduced by viscosity and must be classified as viscous. In this paper, we will confirm numerically that inertial instabilities are also possible in precession-driven flow if the container is spheroidal.

Viscous instability can occur both in the bulk of the fluid and in the Ekman layers (Lorenzani & Tilgner 2001). In the first case, the unstable mode consists of two sets of columnar vortices, one of which is a Rossby wave. In the second case, small-scale structures appear in the boundary layers which easily overstrain the numerical resolution and available computer resources. Control parameters characteristic of the experiments could not be reached because of the onset of the Ekman-layer instability.

Analytical work, on the contrary, has been restricted to inertial instabilities (Kerswell 1993). The response of an ideal fluid in a rotating and precessing ellipsoid is described by a solution usually called the ‘Poincaré solution’ (Poincaré 1910) even though it had been derived 15 years before by Sloudsky (Sloudsky 1895). The Poincaré solution has spatially uniform vorticity. For non-zero ellipticity of the boundaries, the fluid is strained and thereby inertially unstable. The same mechanism acts in rotating bodies subject to tidal deformations and has been reproduced in laboratory experiments (Malkus 1989, Eloy, Le Gal & Le Dizès 2000).

Most of our knowledge about precession-driven flow comes from laboratory experiments with water-filled spheroidal cavities. Experiments by Vanyo *et al.* (1995) and Vanyo & Dunn (2000) have been designed to come as close as possible to the Earth’s parameters. Whereas the characterization of the velocity field was mostly restricted to visualization in older experiments, Noir *et al.* (2001*a*) used acoustic Doppler anemometry and detected internal shear layers which had been predicted theoretically or numerically (Hollerbach & Kerswell 1995; Kerswell 1995; Rieutord & Valdettaro 1997; Tilgner 1999*a*; Noir *et al.* 2001*b*). Here, we will focus on the work by Malkus (1968) who performed experiments with cavities with ellipticities 0.04 and 0.1 at Ekman numbers around 2×10^{-6}. In addition to visualization, Malkus used a torque measurement to determine the amount of energy dissipated in the flow. A sudden jump from somewhat time-dependent to very turbulent flow occurred in the container of ellipticity 0.1 as the precession rate was increased. In the container of smaller ellipticity, the flow became increasingly disordered in a continuous fashion. Intriguingly, the abrupt transition was accompanied by a hysteresis effect: upon decreasing the precession rate, the flow remained turbulent at precession rates at which it was only weakly disordered when the precession rate was increased. At low enough precession rates, of course, turbulence disappeared again. The observed instabilities have initially been interpreted as instabilities of internal shear layers, but they could also be inertial instabilities. In particular, the sudden jump to violent turbulence has been thought to indicate an inertial instability (Kerswell 1993).

The present paper intends to study inertial instabilities numerically. In order to isolate the inertial mechanism, we use free-slip boundary conditions which eliminate the viscous instabilities observed in Lorenzani & Tilgner (2001). Section 2 describes the method employed and § 3 presents the results. In order to get as close as possible to experiments, we reinstall no-slip boundary conditions in § 4, but use the concept of hyperviscosity to suppress the Ekman-layer instability which would otherwise make the simulation unresolvable. The choice of parameters is mostly guided by the desire to interpret the experiments of Malkus (1968). These experiments are more amenable to numerical analysis than later experiments. The results and their implications are summarized in § 5.

2. Mathematical formulation and numerical model

Except for the boundary conditions or the hyperviscosity, the method used here is the same as in Lorenzani & Tilgner (2001). The most important aspects of the method are repeated here in order to make the paper self-contained and to introduce the notation.

The most convenient reference frame for the numerical computation is the frame attached to the rotating and precessing boundaries (the ‘mantle frame’). Within this frame, two coordinate systems will be used: The original one in which the boundaries are ellipsoids of revolution and the computational one in which the boundaries are spherical. The first system will be described with primed symbols. Consider incompressible fluid of kinematic viscosity ν in a spheroidal shell rotating with angular frequency ω_D about the z-axis. The shell furthermore executes precessional motion characterized by the precession vector $\Omega_p \hat{\boldsymbol{\Omega}}_p$ (hats denote unit vectors). The boundaries of the shell are given by:

$$\frac{x'^2}{a^2}+\frac{y'^2}{a^2}+\frac{z'^2}{c^2}=1, \tag{1a}$$

$$\frac{x'^2}{(\eta a)^2}+\frac{y'^2}{(\eta a)^2}+\frac{z'^2}{(\eta c)^2}=1, \tag{1b}$$

$\eta < 1$ and both boundaries have the same ellipticity $e = 1 - c/a$. Units of length and time are chosen as $(1-\eta)a$ and $1/\omega_D$, respectively. Using the same primed symbols as above to denote the dimensionless lengths, the equation of motion for the velocity $\boldsymbol{u}'(\boldsymbol{r}', t)$ reads in a frame of reference attached to the shell:

$$\frac{\partial}{\partial t}\nabla' \times \boldsymbol{u}' + \nabla' \times \{(2(\hat{\boldsymbol{z}}' + \boldsymbol{\Omega}) + \nabla' \times \boldsymbol{u}') \times \boldsymbol{u}'\} = E\nabla'^2 \nabla' \times \boldsymbol{u}' + 2\hat{\boldsymbol{z}}' \times \boldsymbol{\Omega}, \tag{2}$$

$$\nabla' \cdot \boldsymbol{u}' = 0. \tag{3}$$

The Ekman number E is defined by $E = \nu(\omega_D(1-\eta)^2 a^2)^{-1}$ and $\boldsymbol{\Omega} = \Omega_p/\omega_D \hat{\boldsymbol{\Omega}}_p$. The computational coordinate system is now introduced by the transformations:

$$x = x', \qquad y = y', \qquad z = \frac{z'}{1-e}. \tag{4}$$

If the velocities are transformed likewise,

$$u_x = u'_x, \qquad u_y = u'_y, \qquad u_z = \frac{u'_z}{1-e}, \tag{5}$$

we obtain again a solenoidal vector field, $\nabla \cdot \boldsymbol{u} = 0$. The boundaries are now given by:

$$x^2 + y^2 + z^2 = r_o^2, \tag{6a}$$

$$x^2 + y^2 + z^2 = r_i^2, \tag{6b}$$

with $r_i/r_o = \eta$ and $r_o - r_i = 1$. In this paper, we will either use no-slip boundaries in connection with hyperviscosity, or free-slip boundaries. The precession axis $\hat{\boldsymbol{\Omega}}$ forms the angle α $(0 < \alpha < \pi/2)$ with the z-axis and is time-dependent in the chosen system of reference:

$$\hat{\boldsymbol{\Omega}} = \sin\alpha \cos t \ \hat{\boldsymbol{x}} - \sin\alpha \sin t \ \hat{\boldsymbol{y}} + \cos\alpha \ \hat{\boldsymbol{z}}. \tag{7}$$

The equation of motion in the unprimed variables acquires additional terms but it can now be discretized with a spectral method for spherical coordinates. The spatial discretization uses spherical harmonics Y_l^m for the angular variables and Chebychev polynomials for the radius. $\nabla \cdot \boldsymbol{u} = 0$ is satisfied by using a representation in terms of poloidal and toroidal scalars. The time step is a second-order Adams–Bashforth scheme for the nonlinear terms and the Coriolis force coupled to an implicit Euler step for the diffusion term. Technical details of the algorithm are given in Lorenzani & Tilgner (2003).

In this spectral method we solve for expansion coefficients which are indexed by the order l and degree m of the spherical harmonics Y_l^m. Every term in the equations of motion is decomposed into spherical harmonics, including the viscous term. It is convenient to introduce a hyperviscosity into these equations. The hyperviscosity used in spectral methods in spherical geometry is usually a viscosity or an Ekman number which depends on l. If we used hyperviscosity, we replaced E in the equations of motion for the spectral coefficients by E_l given by:

$$E_l = \begin{cases} E, & l \leqslant 10, \\ E\left[1 + \dfrac{0.1}{E}\left(\dfrac{l}{L}\right)^6\right], & l > 10, \end{cases} \tag{8}$$

where L is the highest order of the spherical harmonics retained in the spectral representation of the unknowns. This particular choice will be motivated in § 4.

For the validation of the code, we start from the assumption that the no-slip version has been adequately tested in Lorenzani & Tilgner (2001) and that we only need to verify that the boundary conditions are correct. For that purpose we may as well use a linear problem. Output from the new code has been compared with the independent method used in Tilgner (1999*b*) and good agreement has been found.

3. Simulations with free-slip boundary conditions

As has already been shown in Tilgner (1999*b*), the Poincaré solution with uniform vorticity is a very good approximation to the equations of motion with free-slip boundary conditions for any Ekman number that will be used in this paper. These boundary conditions almost completely eliminate boundary layers, internal shear layers and other deviations from a Poincaré solution which cause the viscous instabilities identified in Lorenzani & Tilgner (2001). Only inertial mechanisms remain to make precession-driven flow unstable in a container with free-slip boundaries.

A useful device to isolate an instability from the basic flow is the symmetry of the velocity field with respect to reflections at the origin (Lorenzani & Tilgner 2001). We split the flow field $\boldsymbol{u}$ in a symmetric ($\boldsymbol{u}_s$) and an antisymmetric ($\boldsymbol{u}_a$) component as:

$$\boldsymbol{u} = \boldsymbol{u}_a + \boldsymbol{u}_s, \quad \boldsymbol{u}_s = (\boldsymbol{u}(\boldsymbol{r}) - \boldsymbol{u}(-\boldsymbol{r}))/2, \quad \boldsymbol{u}_a = (\boldsymbol{u}(\boldsymbol{r}) + \boldsymbol{u}(-\boldsymbol{r}))/2.$$

The basic flow resides entirely in $\boldsymbol{u}_s$ so that $\boldsymbol{u}_a \neq 0$ is a sure indication of an instability. However, an instability does not need to start in $\boldsymbol{u}_a$ but can be excited in $\boldsymbol{u}_s$ as well.

The structure of the excited flow is usually easiest to grasp in a frame of reference denoted with primed coordinates whose z'-axis points along the rotation axis of the fluid (instead of along the symmetry axis of the container). If an approximate validity of the Proudman–Taylor theorem leads to nearly two-dimensional structures, it will be most easily recognized as columns aligned with the z'-axis. The azimuthal wavenumber with respect to the z'-axis will be denoted by m'.

Kerswell (1993) presents a theory of inertial instability which assumes that the strain rates in the Poincaré flow are small (which is realized for small ellipticities and small precession rates). Two sources of instability are identified. The first is introduced by the elliptical shape of the streamlines in the Poincaré solution. The second is because the elliptical streamlines of the Poincaré flow lie in parallel planes and there is shear perpendicular to these planes because the line joining the centres of the ellipses is not perpendicular to the plane of the streamlines. The instability occurs through a triad resonance between the Poincaré flow itself and two inertial modes. The elliptical deformation couples two inertial modes whose azimuthal wavenumber differs by 2 (‘elliptical instability’) whereas the second mechanism (‘shear instability’) couples two inertial modes whose wavenumbers differ by 1. The inertial modes of an ellipsoid are well known. It is thus possible to list all possible resonances involving eigenmodes up to a certain modal degree (Lorenzani 2001). Eigenmodes of higher modal degree are less interesting because they have a higher viscous damping rate and are more difficult to excite in a real fluid. The theory can also make a prediction on the growth rate of a resonant triad in an inviscid fluid which involves a cumbersome integral which depends on the participating eigenmodes. There is, however, a convenient upper bound for the growth rate which depends directly on geometric properties of the Poincaré flow, e.g. its ‘elliptical’ and ‘shear’ strains.

Specific initial conditions have to be chosen for any numerical simulation. This choice is ambiguous for stress free boundaries because all instabilities must eventually die out with free-slip boundary conditions. To see this, we switch momentarily to a ‘precession frame’ of reference chosen such that the precession and rotation axes are stationary, i.e. that this frame is rotating about the precession axis when viewed from inertial space. In the ‘precession frame’, the boundaries merely rotate about the axis of symmetry of the container and therefore do not perform any work on the fluid because the tangential stress at the boundaries vanishes. There is no Poincaré force in this frame and the Coriolis force by definition does not perform any work. We conclude that there is no energy input into the flow. On the other hand, there is dissipation in every container other than a sphere. Poincaré solutions are linear in the Cartesian coordinates and therefore do not dissipate, but they satisfy free-slip boundary conditions only in a sphere or in a spheroid when the rotation axis of the fluid is parallel to the symmetry axis. The general solution in a spheroid must deviate from a Poincaré solution and must dissipate. Dissipation of course also occurs if the flow becomes unstable. Since there is an energy sink and no energy source, the fluid must eventually come to rest in the ‘precession frame’. In the ‘mantle frame’, this final state corresponds to the motion $\boldsymbol{u}' = -\hat{\boldsymbol{z}}' \times \boldsymbol{r}$ which is a solution of (2) for stress-free boundary conditions. However, this solution is stable and of no interest in the present context.

The computations described in this section start from initial conditions which are stationary states on the time scale on which instabilities develop and evolve. The time required to reach the final motion $\boldsymbol{u}' = -\hat{\boldsymbol{z}}' \times \boldsymbol{r}$ is longer for smaller E, whereas inertial instabilities arise also in the limit $E \rightarrow 0$ with a finite growth rate. The initial states used in the following are considered stationary because the rotation axis of the fluid makes oscillations with an opening angle of at most 2° around a mean orientation, and the mean orientation drifts by a couple of degrees from the beginning to the end of a run.

The ambiguity concerning the initial state also sets the scope of these simulations: they are intended to expose generic features of inertial instabilities in flows which are virtually identical to a Poincaré flow, but they cannot relate directly to a specific experiment. A closer connection with experiments is provided by the simulations with hyperviscosity presented in the next section.

We first present a numerical run with the parameters $\alpha = 90^\circ$, $e = 0.15$, $\eta = 0.1$, $\Omega = -0.1$ and $E = 10^{-4}$. The values of α, e and Ω are chosen such that they fall into an instability tongue predicted in Kerswell (1993, figure 3). The variable η is chosen for convenience and E is made reasonably small. The basic state used in Kerswell (1993), equation (4.1), is used here as the initial condition for the time integration. The perturbation theory, which is accurate only for an inviscid fluid at small precession rates, predicts growth in modes with wavenumbers 1 and 2 with a growth rate of 2.7×10^{-2}. In the simulations, we indeed see a growth in the predicted wavenumbers. The instability occurs in the antisymmetric component of the flow field which is zero

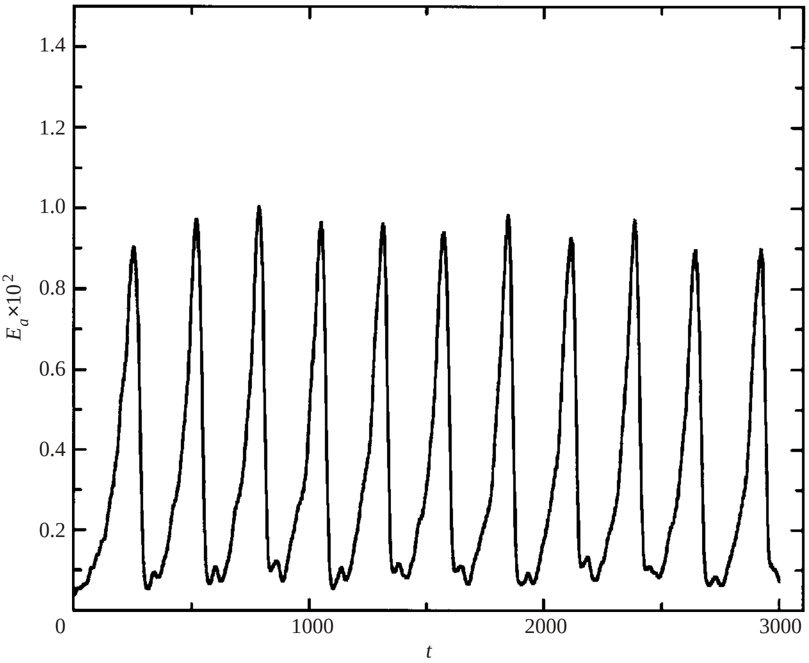

FIGURE 1. Time evolution of the energy E_a contained in the velocity components antisymmetric with respect to reflection at the origin for $\alpha = 90°$, $e = 0.15$, $E = 10^{-4}$ and $\Omega = -0.1$. E_a is zero for a laminar flow.

for the basic flow. The growth rate is 2×10^{-2}. The discrepancy with the theoretical value stated above comes from a finite Ekman number and a precession rate which is not infinitesimal but equal to -0.1. The approximate agreement of the growth rates and the fact that we observe the modes with the expected wavenumber show that we are indeed simulating an inertial instability.

The growing instability does not reach a saturated state but starts to oscillate instead (figure 1). During the growth phases, the instability grows at a rate which is approximately a factor of 2.5 smaller than the linear growth rate of 2×10^{-2} observed at the beginning of the run when the unstable modes still have very small amplitude. This behaviour is reminiscent of the ‘resonant collapse’ observed experimentally by Malkus (1989), Manasseh (1992) and Eloy *et al.* (2000). During resonant collapse, a laminar large-scale inertial mode suddenly decays into small-scale turbulence. The small scales draw energy from the large scales which they dissipate. Once enough energy has been dissipated, the flow becomes laminar and the same instability as before grows once more, only to decay into turbulence again. This cycle repeats indefinitely.

In order to demonstrate quantitatively the connection between our simulation and the resonant collapse phenomenon, we separate the energy E_a contained in $\boldsymbol{u}_a$ into contributions by modes with $m' \leqslant 2$, $m' > 2$ and $m' > 6$. We call the first part ‘large scale’ because it contains the wavenumbers making up the Poincaré flow and the initial inertial instability. The ‘small scales’ must be excited through nonlinearities or further bifurcations. Figure 2 shows the temporal evolution of these energies. There is a phase lag between the oscillations of the large and small scales: the energy in the small scales is maximum when the energy loss of the large scale is fastest, exactly as would be expected for a resonant collapse.

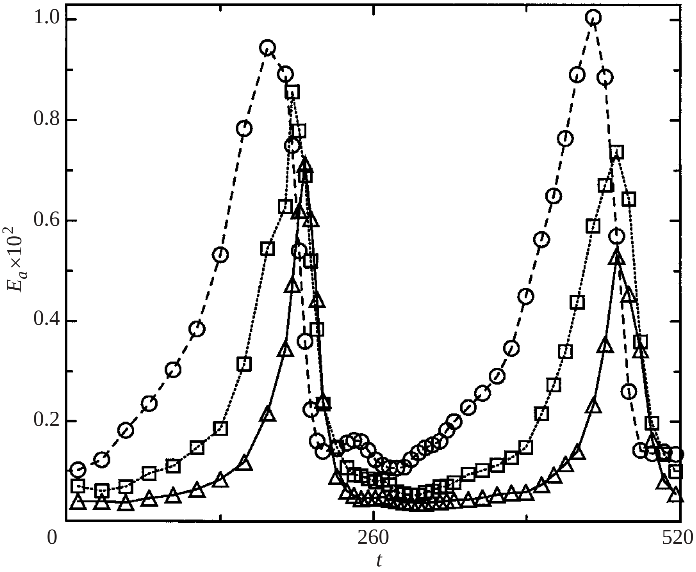

FIGURE 2. Time evolution of the energy E_a contained in all antisymmetric velocity components (circles), in modes with $m' > 2$ (squares, these values have been multiplied by 8), and in modes with $m' > 6$ (triangles, these values have been multiplied by 24) for the same parameters as in figure 1.

An oscillation as shown in figure 1 could also be merely a nonlinear oscillation which does not involve a succession of instabilities as in a resonant collapse. Neither direct simulations nor experiments can draw a strict distinction between both. A resonant collapse is expected to populate higher wavenumbers more than a nonlinear oscillation does, and it is a matter of plausibility whether an experimental or numerical result is classified as one or the other. Another example of an oscillation in the course of which small scales are excited will be presented in figures 5 and 6.

In a second computation, we choose the parameters $\alpha = 30°$, $e = 0.06$, $\eta = 0.1$, $\Omega = -0.14$ and $E = 5 \times 10^{-5}$. Simulations have been started from two different initial conditions, either the Poincaré solution used as basic state in Kerswell (1993), or a flow derived from Busse (1968). All analytical work has been done in the 'precession frame' so that the initial conditions are first obtained in this frame and then transformed into the 'mantle frame' by adding $-\hat{\boldsymbol{z}} \times \boldsymbol{r}$ to the velocity field. For a Poincaré solution $\boldsymbol{u}_P$ given in the 'precession frame', $\boldsymbol{\omega}_F = (1/2)\nabla \times \boldsymbol{u}_P$ is the rotation vector of the fluid. For no-slip boundaries and in the limit of small Ekman and Rossby numbers, Busse (1968) has derived for a spheroid with semi-axes a and c the expression

$$\frac{\boldsymbol{\omega}_F}{\omega_F^2} = \hat{\boldsymbol{z}} + \frac{A\hat{\boldsymbol{z}} \times (\boldsymbol{\Omega} \times \hat{\boldsymbol{z}}) + B(\hat{\boldsymbol{z}} \times \boldsymbol{\Omega})}{A^2 + B^2}, \tag{9}$$

with $A = 0.259(E/\omega_F)^{1/2}(1-\eta) + (1-c/a)\omega_F^2 + \boldsymbol{\Omega}\hat{\boldsymbol{z}}$ and $B = 2.62(E\omega_F)^{1/2}(1-\eta)$, $E = \nu(\omega_D(1-\eta)^2 a^2)^{-1}$. The z-axis points along the symmetry axis of the container. We used (9) with $E = 10^{-15}$ to compute an $\boldsymbol{\omega}_F$ from which a $\boldsymbol{u}_P$ was constructed which then served as the initial condition.

The rotation vectors $\boldsymbol{\omega}_F$ of these two initial conditions differ by an angle of 7°. Both time integrations were run until the first instability started, which involved the

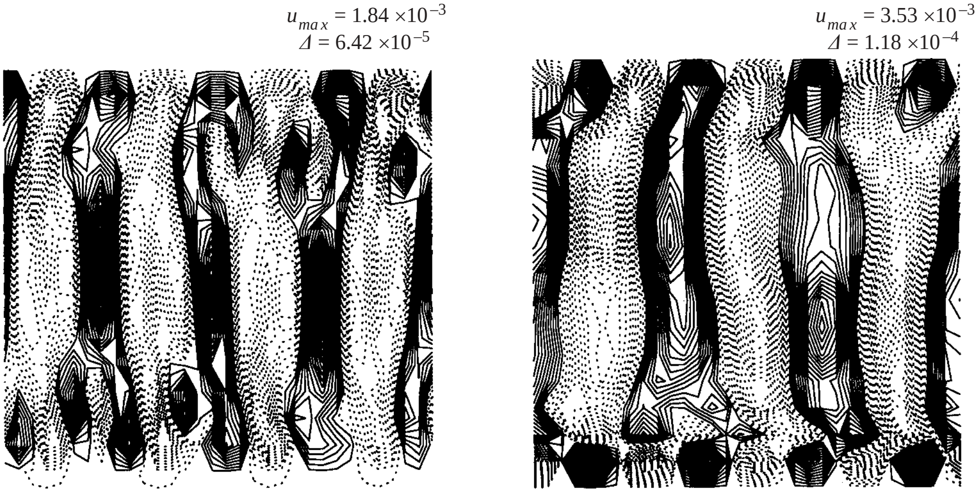

FIGURE 3. u_{sr} (left) and $u_{sz'}$ (right) on cylindrical surfaces at distances 0.44 (left) and 0.34 (right) from the $\boldsymbol{\omega}_F$-axis for $e = 0.06$, $\alpha = 30°$, $\Omega = -0.14$ and $E = 5 \times 10^{-5}$. φ' runs from $-\pi$ to π in going from left to right and θ' varies from $-75°$ to $75°$ (left) and from $-80°$ to $80°$ (right) in going from bottom to top. In this and subsequent figures, continuous and dashed contour lines indicate positive and negative values, respectively. Each panel is labelled with the maximum value u_{max} occurring in the plot together with the spacing of the contour levels Δ.

e	m_a	m_b	λ_a	λ_b	Symmetry	p
0.048	4	5	−0.751	0.249	s	4.5×10^{-3}
0.057	1	2	−0.022	0.978	a	1.0×10^{-3}
0.065	1	3	−0.718	1.282	a	
0.074	3	4	−0.395	0.605	s	1.5×10^{-2}

TABLE 1. List of modes a and b which are exactly resonant in a container of ellipticity e with wavenumbers m and eigenfrequencies λ. The next to last column indicates whether the modes are symmetric (s) or antisymmetric (a) with respect to reflections at the origin. p is the predicted growth rate of the shear instabilities ($|m_a - m_b| = 1$).

same two modes and the same growth rate for both initial conditions. The integration started from the Poincaré solution has then been continued for a much longer time and yielded figures 3–6.

We rely on numerical noise to trigger an instability. During the transient leading to the final state, several different pairs of inertial waves become excited. Initially, the pair $m' = 3$ and 4 appears, followed by $m' = 1$ and 2. Finally, the flow is dominated by a pair with $m' = 1$ and 3 which corresponds to two modes coupled by the elliptical distortion of the streamlines (see table 1).

Following the theory of Kerswell (1993), it is possible to scan the inertial modes for those pairs which are resonant for ellipticities near 0.06 (Lorenzani 2001). The analytical counterparts of the pairs found in the numerics can be identified and are given in table 1. The identification is based on the azimuthal wavenumber and the symmetry of the modes with respect to reflection at the origin.

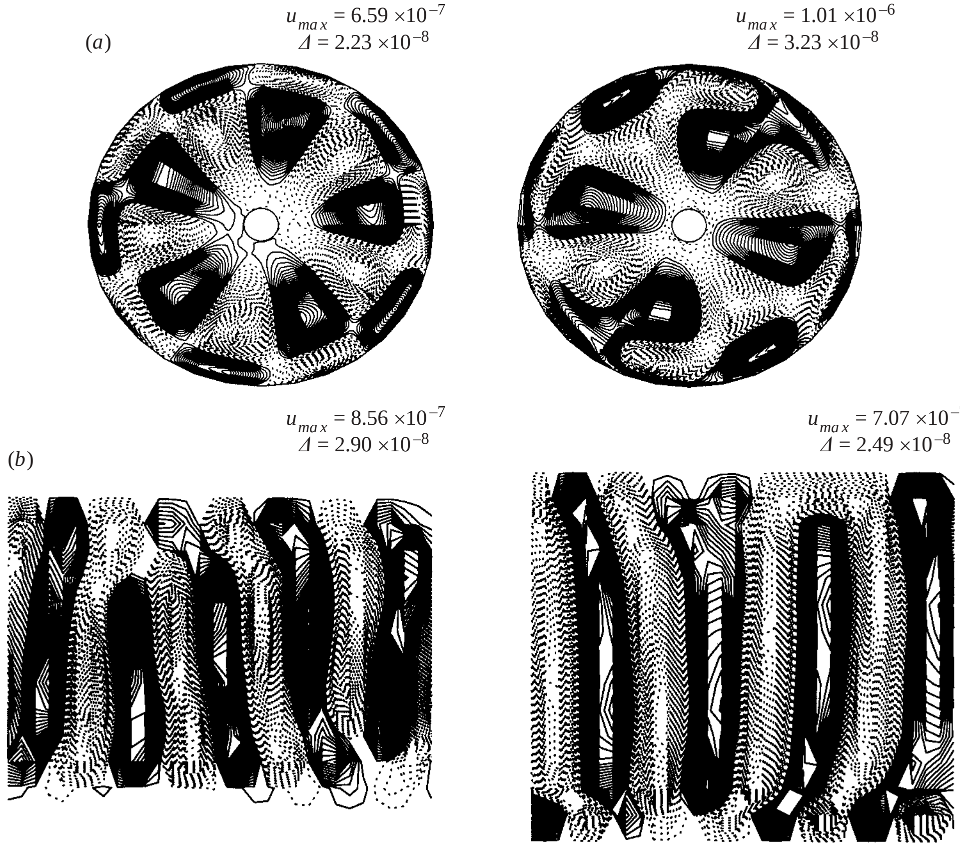

FIGURE 4. Flow for the same parameters as in figure 3 but 2300 units of time later. (*a*) u_{ar} (left) and $u_{az'}$ (right) in the plane perpendicular to $\boldsymbol{\omega}_F$. (*b*) u_{ar} (left) and $u_{az'}$ (right) at distances 0.84 (left) and 0.54 (right) from the $\boldsymbol{\omega}_F$-axis. φ' runs from $-\pi$ to π in going from left to right and θ' varies from $-50°$ to $50°$ (left) and from $-70°$ to $70°$ (right) in going from bottom to top.

Table 1 also gives the growth rates computed from § 2 of Kerswell (1993). It is seen that the pair $m' = 3$ and 4, which dominates the instability in its linear regime, has the largest growth rate. The predicted growth rate of 1.5×10^{-2} compares favourably with the growth rate of 1.2×10^{-2} deduced from the numerical simulation, considering that the theory is for an ideal fluid and infinitesimal shear.

Figures 3 and 4 give an impression of the structure of the flow at various stages of the transient. These are representative of the entire temporal evolution. The graphical representation is of the same sort as in Lorenzani & Tilgner (2001) and is based on figure 10 of that paper: one set of rolls has a vanishing z'-component, the other a vanishing r-component in the equatorial plane. We can therefore conveniently separate both modes by plotting the radial and z'-components of the velocity field. It is important to note that the flow always maintains a columnar structure with columns aligned with the rotation axis of the fluid. It is therefore impossible to distinguish by visual inspection the inertial instabilities described here from the viscous bulk instabilities found in Lorenzani & Tilgner (2001). The sketch in figure 10 of that paper applies to the viscous as well as to the inertial instability. Note that the unstable modes can both be symmetric (figure 3).

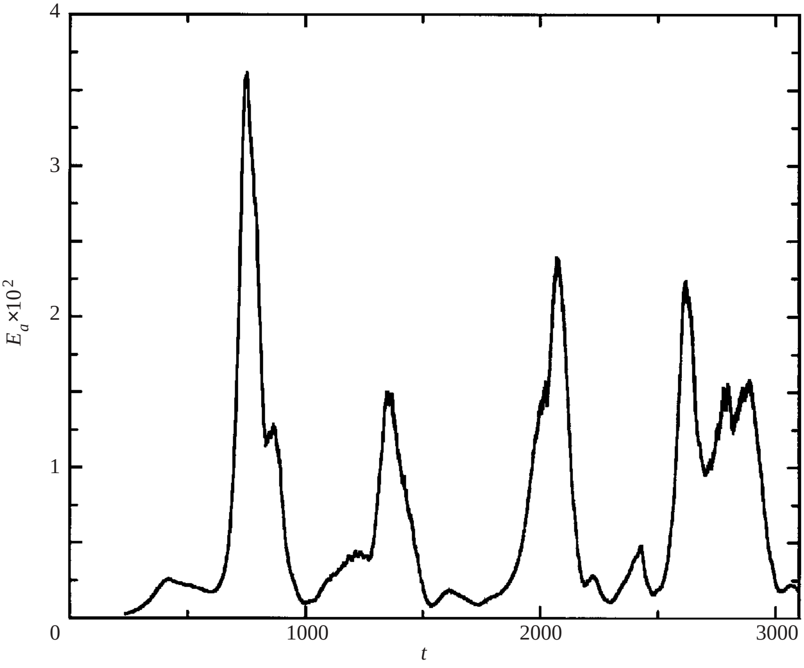

FIGURE 5. Time evolution of the energy E_a contained in the velocity components antisymmetric with respect to reflection at the origin for the same parameters as in figure 3.

A pair $m' = 4$ and 5 appears transiently in the antisymmetric component (figure 4), whereas the only resonance in these wavenumbers at nearby ellipticities is predicted in the symmetric component by the theory (table 1). The origin of this particular pair has not been elucidated.

The flow does not reach a stationary state, but again goes through collapses. For the parameters chosen, the variations of the energy are not periodic any more (figure 5). Figure 6 demonstrates the appearance and disappearance of small-scale structures in the course of the oscillations. The growth rate during the growth phases is roughly 9×10^{-3}.

Laboratory experiments were mostly done with full ellipsoids, but for geophysical applications, the effect of an inner core is of interest. We thus repeat the previous simulation with the same parameters except that we set $\eta = 0.35$. We expect the inner core to cause little change to the resonance conditions because the inertial modes observed without inner core reach their largest amplitude outside the region now occupied by the inner core. And indeed, the numerical simulation reveals an initial instability with the same pair as before ($m' = 3$ and 4) and the final stage is dominated by the pair $m' = 1$ and 3. However, the transients differ (a pair with $m' = 10$ and 11 appears) and no collapses occur, but small scales remain permanently excited in a statistically stationary state at the end of the run (figure 7).

As a summary of this section, we note that the initial phases of simulations with free-slip boundary conditions agree well with theoretical predictions of inertial instabilities of the Poincaré flow. We therefore conclude that the simulated instability is indeed the inertial instability treated in Kerswell (1993). A signature of the elliptical instability is the excitation of two inertial modes whose wavenumbers differ by 2. The shear instability on the other hand cannot be easily distinguished from the viscous

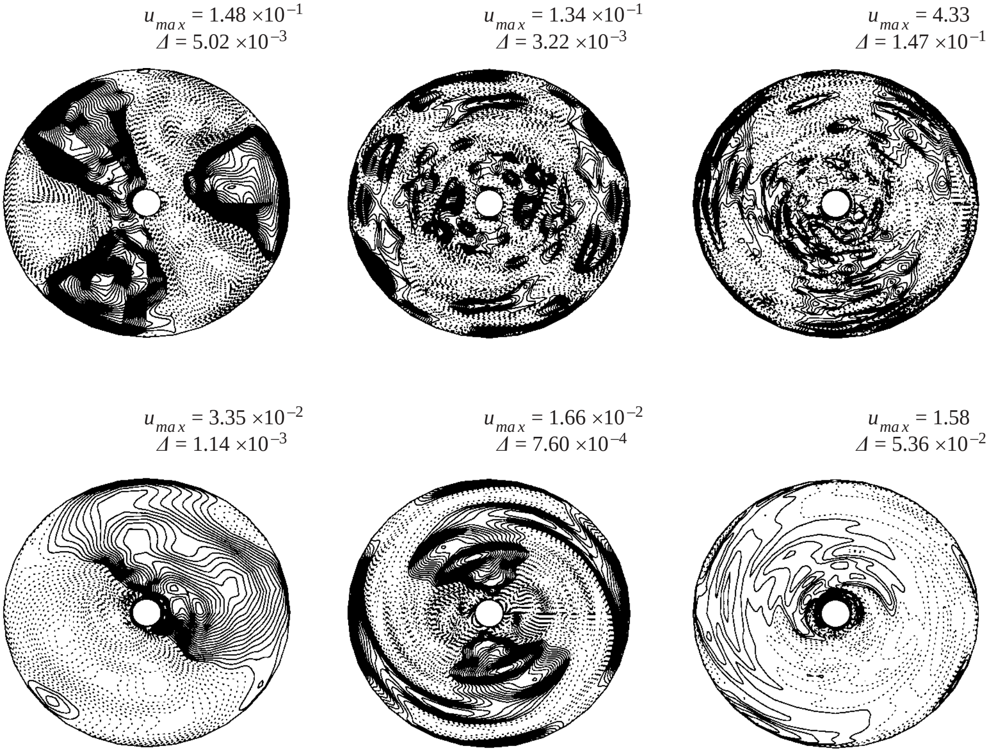

FIGURE 6. Pictures of the flow at the times of the first maximum (top) and the first minimum (bottom) in figure 5. The different panels show u_{ar} (left), $u_{az'}$ (middle) and $(\nabla \times \boldsymbol{u})_{az'}$ (right).

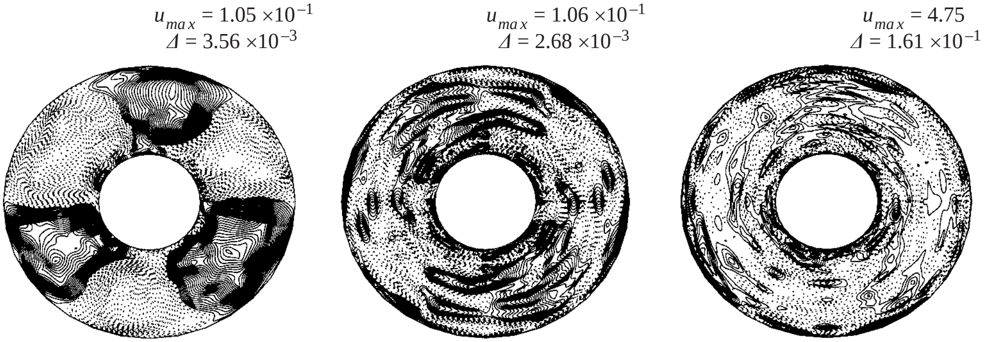

FIGURE 7. u_{ar} (left), $u_{az'}$ (middle) and $(\nabla \times \boldsymbol{u})_{az'}$ (right) for $e = 0.06$, $\alpha = 30°$, $\Omega = -0.14$, $E = 5 \times 10^{-5}$ and $\eta = 0.35$.

instabilities in Lorenzani & Tilgner (2001) since both consist of two sets of columnar rolls whose wavenumbers differ by 1. Figure 10 of Lorenzani & Tilgner (2001) thus summarizes both the inertial shear instability and the viscous bulk instability.

4. Simulations with hyperviscosity

We will now attempt to decide which type of instability acts in Malkus' experiments of 1968. In particular, we seek an interpretation for the hysteretic transition to strongly turbulent flow observed in the container of ellipticity 0.1. For that purpose, we must reintroduce no-slip boundary conditions so that viscous instabilities have a chance to occur, but at the same time, we have to prevent the small-scale instability of the Ekman layer from spoiling any manageable resolution. We thus use the hyperviscosity of equation (8), knowing that we introduce an error in the boundary layers and in the small scales in the bulk should a collapse occur. The errors introduced by hyperviscosity seem acceptable because the boundary-layer instability in Lorenzani & Tilgner (2001) always remained confined to the boundary layer without affecting the bulk. Even though the Reynolds number of the boundary layer surely exceeded its critical value in some experiments, the Ekman-layer instability has never been noted in experiments, which indicates that it stays localized in thin boundary layers also at the parameters typical of experiments. We can therefore consider the dynamics of the Ekman boundary layer to be of secondary importance and tolerate an error there. At the same time, the radial coordinate and the modes making up the Poincaré solution are unaffected by the hyperviscosity (8) so that the orientation of the basic flow is virtually unchanged. The instabilities observed in the previous section involved spherical harmonics of predominantly low order and with small wavenumbers. We thus choose a hyperviscosity which leaves spherical harmonics of order less than 10 unaffected, so that instabilities are little suppressed if they involve modes of low order. Since the excited modes are a superposition of many spherical harmonics, some modification of the critical parameters at which instability sets in necessarily occurs, but we expect to be able to reproduce both viscous and inertial instabilities in a single model.

We start with a container with ellipticity $e = 0.04$ as in Malkus' first experiment. Instead of varying the precession rate at fixed Ekman number as in the experiment, it is advisable in numerical simulations to vary the Ekman number at fixed precession rate because it is then possible to carefully approach the parameter range in which the required resolution overstretches the available computer resources. Note that a hyperviscosity as in (8) does not eliminate thin boundary layers so that a high radial resolution is still necessary at low Ekman numbers.

The parameters for figure 8 are $\alpha = 30°$, $e = 0.04$, $\eta = 0.1$, and $\Omega = -0.035$. In this geometry and at this precession rate, the experiment at $E = 2.5 \times 10^{-6}$ revealed turbulent motion. Decreasing the Ekman number in the simulations starting from 2×10^{-4}, we encounter a first instability with $m' = 1$ and 2. This must be a viscous instability because a comparative run at $E = 10^{-4}$ with free-slip boundary conditions reveals no instability whatsoever. In addition, the behaviour of E_a as a function of the Ekman number is qualitatively the same as in a sphere in which the inertial instabilities cannot exist (see figure 8).

At $E = 2 \times 10^{-5}$, the behaviour of the flow in the ellipsoid changes drastically. The energy of the unstable modes starts to oscillate in a manner typical of the resonant collapse observed for the inertial instabilities in the previous section (figure 9). In the maxima of figure 9, the spectrum of the flow is dominated by $m' = 3$ and 4, whereas during the minima, it is dominated by $m' = 1$ and 2. The most natural interpretation is that an inertial instability has set in on top of the viscous instability. The modes excited by the inertial instability overwhelm the viscously excited ones, but after a collapse, the weak viscously excited modes become visible again. The viscous and inertial instabilities coexist according to this interpretation, the inertially unstable modes having a larger amplitude most of the time.

As a consequence of hyperviscosity, the modes excited by the viscous instability differ from those excited without hyperviscosity at the same parameters in Lorenzani & Tilgner (2001), and the modes excited by the presumed inertial instability

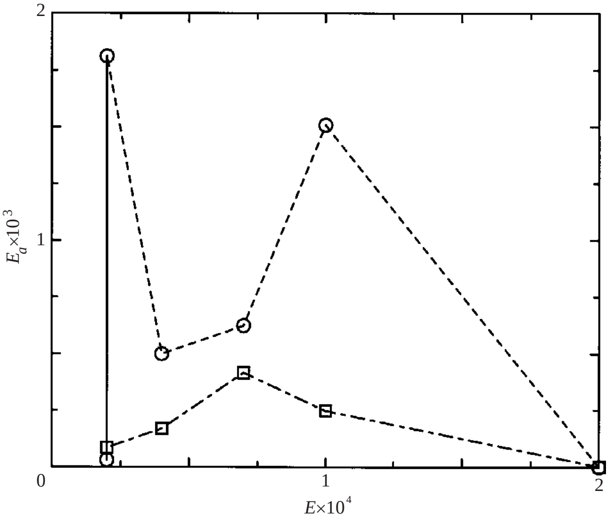

FIGURE 8. The antisymmetric energy E_a as a function of the Ekman number E for $\Omega = -3.5 \times 10^{-2}$, $e = 0.04$, $\alpha = 30°$, $\eta = 0.1$ (circles) and $\Omega = -0.1$, $e = 0$, $\alpha = 40°$, $\eta = 0.1$ (squares). The broken lines are guides to the eye through the data points. The continuous line connects two points at $E = 2 \times 10^{-5}$ which give the maximum and minimum values visited during the oscillations shown in figure 9.

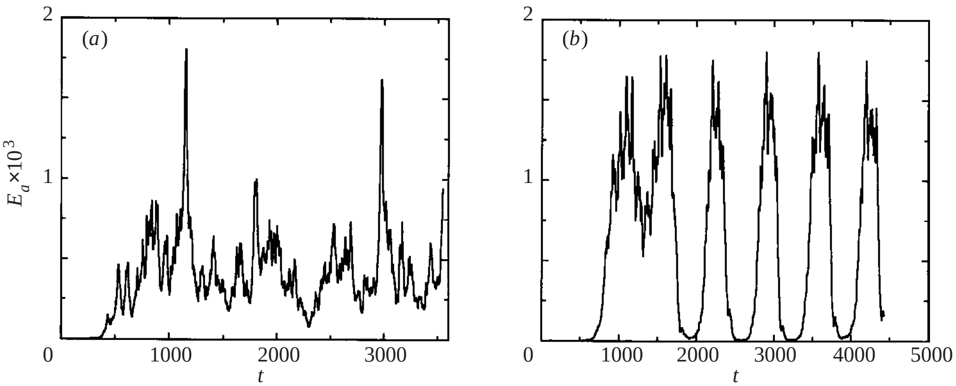

FIGURE 9. Time evolution of E_a for (*a*) $E = 4 \times 10^{-5}$ and (*b*) $E = 2 \times 10^{-5}$. The other parameters are the same as for the circles in figure 8, i.e. $\Omega = -3.5 \times 10^{-2}$, $e = 0.04$, $\alpha = 30°$, and $\eta = 0.1$.

do not correspond to any identifiable triad resonance at nearby parameters. In order to further support the classification of this instability, we could, in principle, track its onset as a function of E. However, this undertaking is utopian considering the available computer resources. With these caveats, it is nonetheless plausible to assume that Malkus observed an inertial instability in his experiment.

Another experiment in Malkus (1968) used an ellipsoid with $e = 0.1$ and showed a remarkable jump in the dissipated energy as a function of precession rate together with a hysteresis. In order to reproduce this behaviour, we have to drop our strategy of varying E. Instead, we keep E fixed at $E = 7 \times 10^{-5}$ and vary Ω. The result is given in table 2. A sudden jump in the antisymmetric energy by more than an order of

Ω	E_a	θ_F (deg.)	$\lvert\omega_F\rvert$
–0.055	2.37×10^{-4}	33.95	0.877
–0.06	6.25×10^{-4}	41.22	0.798
–0.065	1.45×10^{-2}	81.49	0.292

TABLE 2. The energy in the antisymmetric modes E_a, the angle between container and fluid axes θ_F, and the angular velocity of the fluid $|\boldsymbol{\omega}_F|$ as a function of the precession rate Ω for $e = 0.1$, $\alpha = 90°$, and $\eta = 0.1$. The hyperviscosity (8) was used with $E = 7 \times 10^{-5}$.

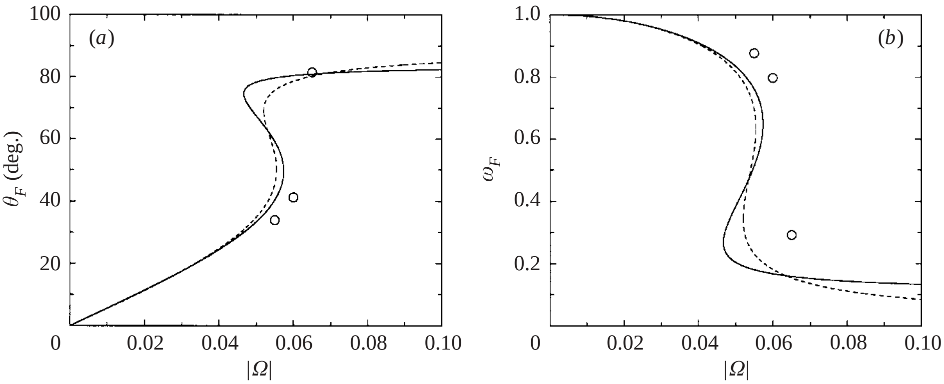

FIGURE 10. The angle between the fluid and the container axes, (a) θ_F and (b) $\omega_F = |\boldsymbol{\omega}_F|$ as a function of $|\Omega|$. The continuous lines result from using equation (9) for $E = 2 \times 10^{-6}$, $e = 0.1$, $\alpha = 96°$, and $\eta = 0$. The circles are numerical simulations, and the dashed line solutions of (9), for $E = 7 \times 10^{-5}$, $e = 0.1$, $\alpha = 90°$, and $\eta = 0.1$.

magnitude is observed when increasing $|\Omega|$ beyond $\Omega \approx -0.06$. After the transition, the flow consists mainly of small-scale motion.

The variation in E_a and the hysteresis have nothing to do with the onset of a new instability but are rather a manifestation of a reorientation of the vorticity of the underlying Poincaré flow. Figure 10 shows the angle θ_F between the axes of the container and the fluid. This angle abruptly increases at $\Omega \approx -0.06$. At the same time, the flow in the bulk (which has nearly uniform vorticity below the transition) strongly departs from a Poincaré flow (see figure 11). Accordingly, higher strain occurs above than below the transition which explains the sudden increase of the antisymmetric energy.

The mechanism behind the transition already appears in Busse's (1968) theory leading to (9). As pointed out in Noir (2000), this equation can have multiple solutions. Figure 10 shows all possible solutions for Malkus' experiment which showed the hysteresis. Starting from $\Omega = 0$, we follow a branch (only one exists at low Ω) which suddenly stops existing and forces the flow to switch to the upper branch. We find the transition at $\Omega = -0.057$, whereas Malkus indicates the range $|\Omega| = 0.047 - 0.057$. The presence of two branches readily explains the hysteresis. The upper and lower branches coexist for $-0.047 > \Omega > -0.057$ according to the asymptotic theory, so that the flow can stay on the upper branch if $|\Omega|$ is reduced from $|\Omega| > 0.057$ to $|\Omega| < 0.057$ until the lower branch is recovered at $\Omega = -0.047$. Malkus was able to follow the upper branch down to $\Omega = -0.03$. This discrepancy may be due to the fact

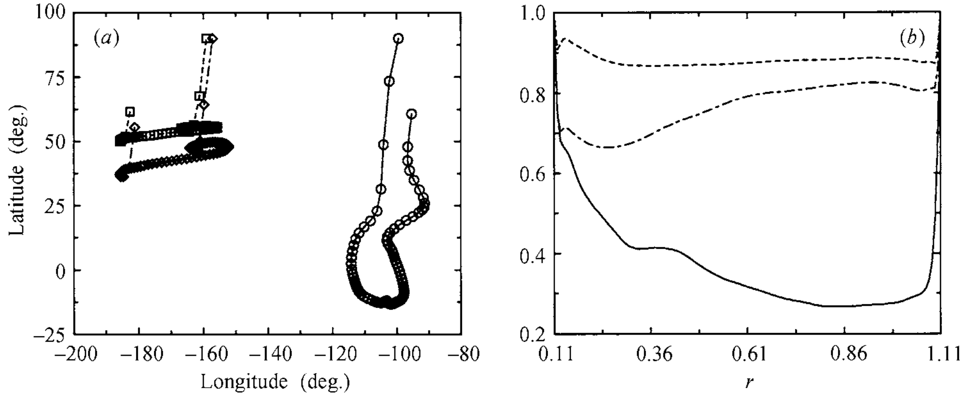

FIGURE 11. (*a*) Latitude and longitude of the direction of the rotation vector $\boldsymbol{\omega}(r)$ of the fluid shell at radius r. $\boldsymbol{\omega}(r)$ is given by $\boldsymbol{\omega}(r)=(1-e+1/(1-e))[-\mathrm{Re}\{W_1^1(r)\}\hat{\boldsymbol{x}}+\mathrm{Im}\{W_1^1(r)\}\hat{\boldsymbol{y}}]+W_1^0(r)\hat{\boldsymbol{z}}+\hat{\boldsymbol{z}}$ (see Lorenzani & Tilgner 2001). The three curves correspond to $\Omega=-0.055$ (squares), −0.06 (diamonds) and −0.065 (circles). The other parameters are as in figure 10, $E=7\times10^{-5}$, $e=0.1$, $\alpha=90°$, and $\eta=0.1$. The symbols mark the direction of $\boldsymbol{\omega}(r)$ at the radii $r_i+(r_o-r_i)/41n$, $n=1\cdots41$. The axis of (retrograde) precession points at zero longitude and a latitude of 0°. (*b*) ω, the absolute value of $\boldsymbol{\omega}(r)$ as a function of r for the same parameters as in (*a*) with the precession rates $\Omega=-0.055$ (dashed), −0.06 (dot-dashed) and −0.065 (solid).

that the flow on the upper branch is highly turbulent and far away from a state with constant vorticity, at variance with the assumptions of Busse (1968).

In the previous paragraph, we have used (9) far beyond its formal range of applicability. Past experience (Tilgner 1999*a*; Lorenzani & Tilgner 2001; Tilgner & Busse 2001) has shown, however, that (9) yields satisfactory results even for large tip-over angles and precession rates, so that it seems reasonable to compare Malkus' experimental results with (9). However, there remains the possibility that multiple solutions of (9) arise only because it is used for parameters which violate the assumptions leading to (9).

5. Discussion

This paper has presented simulations of precession-driven flows under circumstances in which inertial instabilities occur. The classification as inertial instability is unambiguous if free-slip boundary conditions are used, because the basic flow is then lacking the interior shear layers and distortions which lead to other types of instability. The inertial instabilities can again be separated into two classes: shear and elliptical instabilities, which excite pairs of inertial modes whose azimuthal wavenumbers differ by one and two, respectively. The shear instability is indistinguishable by mere visual inspection from the viscous bulk instability found in Lorenzani & Tilgner (2001). Both consist of two sets of rolls, one being a set of vortices antisymmetric with respect to the equatorial plane, the other set being symmetric. When no-slip boundary conditions are used, it is in practice impossible to classify an instability as inertial shear instability or as viscous bulk instability with absolute certainty. The distinction between these types of instability is, however, of interest because we have a theoretical understanding of the inertial mechanism and can thus extrapolate its properties to Earth's parameters.

During the growth phase, different pairs of modes may appear in the course of time if various triads are close to resonance. At saturation, the flow may permanently contain small scales and be as close to a turbulent flow as a well-resolved simulation can be, or the flow may go through collapses, i.e. that periodically an instability grows until the flow becomes turbulent, after which it relaminarizes, so that the instability can grow again and decay into turbulence once more. Collapses are commonly observed in experiments with rotating deformed containers which are intended to be models of tidally distorted bodies, but experiments with precessing ellipsoids only revealed permanently turbulent flow. Our simulations show that collapses can also occur in precessing ellipsoids of small ellipticity. The numerical data also reveal how energy is transferred from large to small scales during a collapse (figure 2).

The vigorous motions observed in the experiments by Malkus (1968) are likely to be inertial rather than viscous instabilities. This does not exclude the possibility of a viscous instability appearing first at low precession rates. In one case, Malkus has observed a spectacular transition from a chaotic to a fully turbulent flow accompanied by a hysteresis effect. This transition is readily explained if we assume that Busse's asymptotic theory leading to (9) is still valid for the parameters of the experiment. Indeed, the orientation of the basic flow may change abruptly as a function of the precession rate. When this happens, the strain in the basic flow changes equally abruptly and causes the transition from a more to a less stable flow. In addition, several orientations of the flow may exist for a given precession rate which explains the hysteresis phenomenon.

We finally apply the above results to the Earth. A catastrophic reorientation as observed in Malkus' experiment is not relevant to the Earth. For $E = 10^{-15}$, $\alpha = 23.5^\circ$ and $e = 1/400$ a similar transition occurs only at $\Omega \approx -10^{-3}$, whereas the actual precession rate of the Earth is $\Omega \approx -10^{-7}$. For the Earth's parameters, Kerswell's criterion should be appropriate because the basic flow he assumes is close to the one predicted by (9). According to that criterion, the state of precession-driven flow in the Earth's core is uncertain because commonly accepted values of the viscosity of the core put the flow close to its stability limit. Fluid viscosity is, however, one of the least well-constrained material properties of the core. Let us assume that the core is unstable. Precession then possibly drives the geodynamo or at least contributes to the secular variation of a convectively driven dynamo. In the latter case, the collapse phenomenon is of special interest. When collapse occurred in our simulations, the growth rate after the collapse was within a factor of 2–3 from the growth rate, the same modes have during a linear growth phase starting from a Poincaré solution as described by perturbation theory. Using the upper bound for the growth rate of an inertial instability given by Kerswell (1993) applied to Earth's numbers gives a growth rate of $(20\,000 \text{ year})^{-1}$. Viscosity also acts to slow this growth. If collapses play a role in the Earth's core, they could manifest themselves in variations of the magnetic field with a time constant of 20 000 years or longer.

This work was supported by the 'Deutsche Forschungsgemeinschaft'. Most of the simulations presented here have been run on the CRAY T3E parallel machines of the High Performance Computing Center Stuttgart.

REFERENCES

Bullard, E. 1949 The magnetic field within the earth. *Proc. R. Soc. Lond.* A **197**, 433–453.

Busse, F. 1968 Steady fluid flow in a precessing spheroidal shell. *J. Fluid Mech.* **33**, 739–751.

Eloy, C., Le Gal, P. & Le Dizès, S. 2000 Experimental study of the multipolar vortex instability. *Phys. Rev. Lett.* **85**, 3400–3403.

Hollerbach, R. & Kerswell, R. 1995 Oscillatory internal shear layers in rotating and precessing flows. *J. Fluid Mech.* **298**, 327–339.

Kerswell, R. 1993 The instability of precessing flow. *Geophys. Astrophys. Fluid Dyn.* **72**, 107–144.

Kerswell, R. 1995 On the internal shear layers spawned by the critical regions in oscillatory Ekman boundary layers. *J. Fluid Mech.* **298**, 311–325.

Lorenzani, S. 2001 Fluid instabilities in precessing ellipsoidal shells. PhD thesis, University of Göttingen.

Lorenzani, S. & Tilgner, A. 2001 Fluid instabilities in precessing spheroidal cavities. *J. Fluid Mech.* **447**, 111–128.

Lorenzani, S. & Tilgner, A. 2003 Inertial instabilities in precession driven flow. In *High Performance Computing in Science and Engineering 2002* (ed. E. Krause & W. Jäger). Springer.

Malkus, V. 1968 Precession of the earth as the cause of geomagnetism. *Science* **160**, 259–264.

Malkus, V. 1989 An experimental study of global instabilities due to the tidal (elliptical) distortion of a rotating elastic cylinder. *Geophys. Astrophys. Fluid Dyn.* **48**, 123–134.

Manasseh, R. 1992 Breakdown regimes of inertia waves in a precessing cylinder. *J. Fluid Mech.* **243**, 261–296.

Noir, J. 2000 Ecoulements d'un fluide dans une cavité en précession: approches numérique et expérimentale. PhD thesis, Université Joseph Fourier, Grenoble.

Noir, J., Brito, D., Aldridge, K. & Cardin, P. 2001*a* Experimental evidence of inertial waves in a precessing spheroidal cavity. *Geophys. Res. Lett.* **38**, 3785–3788.

Noir, J., Jault, D. & Cardin, P. 2001*b* Numerical study of the motions within a slowly precessing sphere at low Ekman number. *J. Fluid Mech.* **437**, 283–299.

Poincaré, H. 1910 Sur la précession des corps déformables. *Bull. Astronom.* **27**, 321–356.

Press, W., Teukolsky, S., Vetterling, W. & Flannery, B. 1986 *Numerical Recipes*. Cambridge University Press.

Rieutord, M. & Valdettaro, L. 1997 Inertial waves in a rotating spherical shell. *J. Fluid Mech.* **341**, 77–99.

Sloudsky, T. 1895 De la rotation de la terre supposée fluide à son intérieur. *Bulletin de la Société Impériale des Naturalistes* **9**, 285–318.

Tilgner, A. 1999*a* Magnetohydrodynamic flow in precessing spherical shells. *J. Fluid Mech.* **379**, 303–318.

Tilgner, A. 1999*b* Non-axisymmetric shear layers in precessing fluid ellipsoidal shells. *Geophys. J. Intl* **136**, 629–636.

Tilgner, A. & Busse, F. 2001 Fluid flows in precessing spherical shells. *J. Fluid Mech.* **426**, 387–396.

Vanyo, J. & Dunn, J. 2000 Core precession: flow structures and energy. *Geophys. J. Intl* **142**, 409–425.

Vanyo, J., Wilde, P., Cardin, P. & Olson, P. 1995 Experiments on precessing flows in the earth's liquid core. *Geophys. J. Intl* **121**, 136–142.